Microwave-assisted synthesis of thermoelectric oxides and chalcogenides

Marta María González-Barrios [a], Marina Tabuyo-Martínez [a], Vanessa Cascos [a,b], Óscar Juan Durá [c], José Antonio Alonso [b], David Ávila-Brande [a], Jesús Prado-Gonjal [a,*]

[a] Departamento de Química Inorgánica, Universidad Complutense de Madrid, E-28040, Madrid, Spain
[b] Instituto de Ciencias de Materiales de Madrid (ICMM). Consejo Superior de Investigaciones Científicas (CSIC). Sor Juana Inés de La Cruz 3, E-28049, Madrid, Spain [c] Departamento de Física Aplicada, Universidad de Castilla-La Mancha, Ciudad Real, E-13071, Spain

A B S T R A C T

The combination of microwaves with other classical synthetic methods may be considered as a powerful tool for the preparation of metal oxides and metal chalcogenides. This approach allows the modification of the reaction kinetic significantly by shortening the processing time to minutes and it minimizes the energy consumption during the synthesis. In this work, potential thermoelectric compounds, which enable the direct conversion of temperature gradients into useful electric energy, have been produced by means of microwave-chemistry routes. Pure phases of $SnS_{1-x}Se_x$ (x = 0, 0.2, 1) have been synthesized in just 1 min by using microwave-hydrothermal synthesis. Moreover, $Zn_{0.98}M_{0.02}O$ (M = Al, Ga) rods were formed by microwave-coprecipitation method in 5 min. Besides, 8 min of microwave-heating were enough for the combustion of $Sr_{1-x}La_xTiO_{3-\delta}$ (x = 0, 0.05, 0.1). In all cases, the utilization of microwave radiation produces high-quality phases. A comprehensive study of the structural, microstructural and thermoelectric properties of the microwave-synthesized materials is here per-formed by means of X-ray diffraction, SEM, HRTEM and temperature dependence measurements of Seebeck coefficient, electrical conductivity and thermal conductivity.

Keywords:
Microwave-synthesis
Energy
Thermoelectrics
Oxides
Chalcogenides

1. Introduction

A dramatic transition to a more sustainable energy system is required to achieve a net zero carbon emissions by 2050 [1,2]. Scientific community is making a great effort for the improvement of the efficiency of any kind of energy generation process. For that, and 200 years after Thomas Seebeck reported his discovery of thermoelectricity (August 16, 1821) [3]. Thermoelectric devices -which transform heat given off from multiple sources (*i.e.* power plants, heavy industry, automotive sector, electronic devices, human body …) into electrical power- may provide part of the solution to diminish the environmental emergency and energy requests [4,5]. Approximately 2/3 of the worldwide-applied energy carriers are converted into waste-heat, so the retrieval of a part of this waste-heat -by means of the Seebeck effect-leads to extensive energy saving [6].

Seebeck effect consists of the generation of an electrical current in a circuit (driven by ΔV) when a temperature difference (ΔT) exists at the ends of a material (equation (1)). This is produced by a higher average velocity (in absolute terms) of the charge carriers in the hotter part of the sample, producing an effective diffusion towards the cold part [5].

$$S = - \Delta V / \Delta T \quad \text{(eq.1)}$$

The conversion efficiency of thermoelectric devices, which are based on couples of *n*-type and *p*-type semiconductors electrically connected in series and thermally in parallel, lies directly in the thermal and electrical features of the constituent semiconducting materials. The material's performance is defined by the dimensionless figure of merit zT (equation (2)), which depends on the Seebeck coefficient (S), electrical resistivity (ρ), absolute temperature (T) and thermal conductivity (κ). The latter is composed of electronic (κ_e) and lattice vibration (κ_L) contributions [7,8].

$$zT = \frac{S^2}{\rho \cdot \kappa} T = \frac{S^2}{\rho \cdot (\kappa_e + \kappa_l)} T \quad \text{(eq. 2)}$$

Therefore, the highest thermoelectric performance of a material is given by the conjunction of a simultaneously low electrical resistivity and low thermal conductivity with a high Seebeck coefficient [35]. Unfortunately, due to the interconnection between all these thermoelectric properties, achieving materials with a high thermoelectric performance is not an easy task. While zT values ≈ 1 are reached by

* Corresponding author.
E-mail address: jpradogo@ucm.es

commercial thermoelectrics (*i.e.* Bi_2Te_3, PbTe, SiGe), recent progress has led to the synthesis of novel compounds with zT values above unity: Skutterudites [9–11], half-Heusler [12,13], Si–Ge alloys [14], clathrates [15] and metal chalcogenides [16,17] are examples of new advanced families of compounds with high thermoelectric performance [18]. Among all of them, an appealing phase is SnSe, as it has been reported a zT value of 2.6 at 923 K along the *b*-crystallographic axis in the single-crystal form [19]. This exceptional figure of merit is explained in terms of its ultralow thermal conductivity and the high power factor attributed to the presence of multiple bands in the electronic band structure, improving the charge transport. Nevertheless, zT values for polycrystalline SnSe are generally lower than 1, due to a higher electrical resistivity and higher thermal conductivity. Therefore, there is a remarkable interest to achieve similar values as for the single crystal and, recently, Zhou et al. described an outstanding zT value of 3.1 at 783 K for a polycrystalline $Na_{0.03}Sn_{0.965}Se$ sample [20].

In addition to developing compounds with competitive zT values, the search for inexpensive and environmentally-friendly materials is essential. SnS phase is a stimulating starting point as it is isoelectronic and isostructural to SnSe but Sulfur is more abundant (260 ppm in Earth's crust), less toxic and cheaper than Selenium (0.05 ppm in Earth's crust). Previous publications show zT values $\leq$ 0.6 for polycrystalline SnS [21,22]. However, the modification of the carrier concentration by generating Sn vacancies or doping could be adequate strategies to improve its thermoelectric properties [23].

Even though these metal chalcogenides exhibit decent thermoelectric efficiencies, their application for waste-heat recovery is restricted due to their poor chemical stability, superficial oxidation or possible sublimation, which limit their use at high temperatures. To avoid these problems, it is necessary to find stable ceramics, such as metal oxides, where oxidation is not an issue [24]. However, most of the well-known oxides present low carrier mobility and high thermal conductivity, limiting their use for thermoelectric applications. Despite that, there are some families of oxides that are worth studying for thermoelectric applications: $Na_xCo_2O_4$ [25–28], $CaMnO_3$ [29,30], Al-doped ZnO [31,32] or $SrTiO_3$-based materials [33–36].

Metal chalcogenides and metal oxides are commonly prepared by extended annealing processes (days) of stoichiometric amounts of high-purity precursors at high temperatures [37]. The use of this method involves the need for high temperatures to accelerate diffusion, intermediate grindings, high energy and time consumption. In the case of metal chalcogenides, additionally, it is necessary to work in an evacuated sealed tube to avoid oxidation. Consequently, there is currently growing research of alternative synthetic routes where time and temperature of the process are minimized.

The main difference between microwave heating and conventional heating is that, in the latter, the heating mechanism involves convection or conduction processes, consequently taking more time to achieve the target temperature in the reaction mixture due to thermal gradients (the walls being hotter than the inside). On the other hand, the alternating electromagnetic field of microwaves interacts with matter on a molecular level, producing an extremely rapid heating rate and uniform heating [38]. The efficiency of this heating depends mainly on the dielectric properties of the species involved in the reaction. Dielectric or polar compounds are considered as absorbing materials, as they are able to transform the electromagnetic energy efficiency into heat [39,40]. Metals or materials with a high electrical conductivity reflect the microwave radiation and do not allow deeper penetration of the electromagnetic wave, while insulators or materials with low dielectric permittivity are transparent to microwaves as the absorption of microwave energy due to dielectric polarization is low [41].

In this work, it is shown that tin chalcogenides (SnS, SnSe, $SnS_{0.8}Se_{0.2}$) and metal oxides ($Zn_{0.98}Al_{0.02}O$, $Zn_{0.98}Ga_{0.02}O$; $SrTiO_{3-\delta}$, $Sr_{0.95}La_{0.05}TiO_{3-\delta}$, $Sr_{0.9}La_{0.1}TiO_{3-\delta}$) can be easily synthesized by means of ultrafast microwave routes. A combination of microwaves with other conventional methods, such as hydrothermal, coprecipitation or combustion is explored for the preparation of these thermoelectric phases. Furthermore, structural and microstructural characterization by X-ray diffraction (Rietveld refinement), high resolution transmission electron microscopy and scanning electron microscopy have been performed. Besides, a detailed investigation of the thermoelectric properties and their correlation with the structure of the materials is also presented.

2. Materials and methods

2.1. Synthesis and sintering

2.1.1. Preparation of tin chalcogenides by microwave-hydrothermal synthesis

Microwave-assisted hydrothermal synthesis provides the advantages of microwave and hydrothermal methods. The latter achieves moderate pressures (autogenous pressure) when heating the system at temperatures over 100 °C (usually between 100 °C and 220 °C). The kinetics of solution–crystallization is increased by the coupling of the electromagnetic wave to the polar molecules of the solution contained in a closed reaction system [42]. Besides the typical parameters controlled in hydrothermal synthesis (*i.e.* time, pressure, temperature, pH), this process involves additional monitoring of the microwave power. Commercial equipment regulates the microwave power according to the reaction program automatically. Power is instantaneously cut off when the programmed temperature is reached and connected again if it is necessary to increase the temperature to follow the programmed heating ramp.

In this work, a commercial Milestone ETHOS 1 instrument, fully automatized and operating at 2.45 GHz, was used for the synthesis of SnS, SnSe and $SnS_{0.8}Se_{0.2}$. This equipment allows the control of the reaction parameters (*i.e.* power–temperature, time and pressure) and it is equipped with a stirrer motor, which improves the homogeneity of the reaction mixture, preventing the formation of hot-spots that could damage the vessel.

The proposed phases were synthesized by mixing two solutions: (Solution 1) 8 mmol of $SnCl_2$ (Scharlau, 99.5%) were added to 40 mL of a NaOH 1.2 M (Sigma-Aldrich, ≥98%). (Solution 2) 4 mmol of S (precipitate, Scharlau, 99.5%) or Se (powder, Sigma-Aldrich, 99.5%) were dissolved in 20 mL of ethylene glycol (Sigma-Aldrich, anhydrous, 99.8%) and stirred for 30 min. Then, 5 mL of hydrazine monohydrate 64–65% (Sigma-Aldrich, 98%), which is the reducing agent, were added dropwise to the solution. The prepared solutions were mixed and placed into a PTFE vessel. A carrousel with two vessels was situated in the microwave in order to replicate the synthesis twice at the same time. The vessels were instantly heated by microwaves at 180 °C for just 1 min (heating rate ≈ 36 °C/min). The autogenous pressure of the system was *ca.* 13 bars and power was limited to 500 W, although the maximum power employed by the equipment at these conditions was *ca.* 350 W. Once the system is cooled down, *ca.* 0.6 g of black polycrystalline powder formed in the autoclave was washed with distilled water and dried in a vacuum line (10^{-3} mbar) at 80 °C for 5 h to avoid surface oxidation of the particles.

2.1.2. Preparation of $Zn_{0.98}M_{0.02}O$ (M = Al, Ga) by microwave-coprecipitation synthesis

Coprecipitation method requires the preparation of a solution of the starting reactants and the addition of a precipitating agent. Generally, it is necessary to heat the solution at low temperatures (below 100 °C) to start the precipitation process and the formation of the required product. In this case, $Zn_{0.98}M_{0.02}O$ (M = Al, Ga) compounds were formed by combining the soft-chemistry coprecipitation method and heating by microwave radiation. Stoichiometric amounts of $Zn(NO_3)_2{\cdot}6H_2O$ (Sigma-Aldrich, >99%), $Al(NO_3)_3{\cdot}9H_2O$ (Sigma-Aldrich, >98%) or $Ga(NO_3)_3{\cdot}xH_2O$ (Sigma-Aldrich, >98%) and hexamethylenetetramine (Sigma-Aldrich >99.0%) –to form 8 mmol of product - were dissolved in 70 ml deionized water and added into a PTFE vessel. The use of

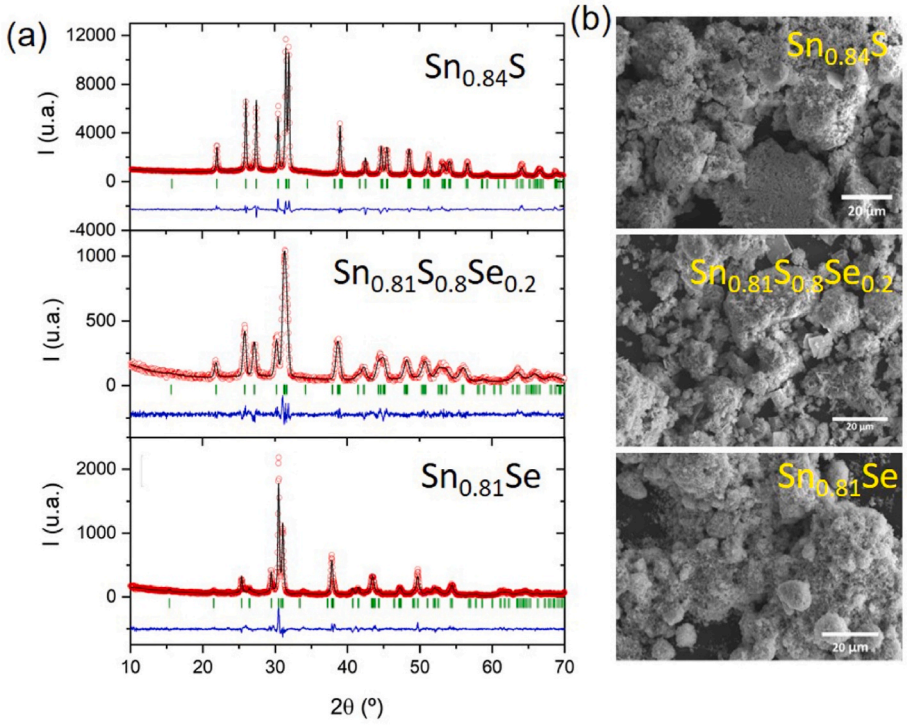

Fig. 1. (a) X-ray diffraction patterns at room temperature of microwave-synthesized $Sn_{0.84}S$, $Sn_{0.81}S_{0.8}Se_{0.2}$ and $Sn_{0.81}Se$, refined in orthorhombic *Pnma* space group: Observed (red circles), calculated (black line) and difference (blue line) profiles. Bragg positions are indicated as green vertical lines. (b) SEM micrographs of $Sn_{0.84}S$, $Sn_{0.81}S_{0.8}Se_{0.2}$ and $Sn_{0.81}Se$ powder. (For interpretation of the references to colour in this figure legend, the reader is referred to the Web version of this article.)

Table 1
Refined structural parameters obtained from powder X-ray diffraction for $Sn_{0.84}S$, $Sn_{0.81}S_{0.8}Se_{0.2}$ and $Sn_{0.81}Se$ at room temperature (*Pnma* space group). (Refinement agreement factors: R_{Bragg} $Sn_{0.84}S$ = 2.45%; R_{Bragg} $SnS_{0.8_1}Se_{0.2}$ = 3.70%; R_{Bragg} $Sn_{0.81}Se$ = 3.67%).

	Space Group	*a*/Å	*b*/Å	*c*/Å	Atom	x	y	z	Occ	U_{iso}/Å^2
$Sn_{0.84}S$	***Pnma***	11.2052(9)	3.9867(3)	4.3265(4)	Sn	0.117(5)	0.25	0.099(1)	0.835(7)	0.016(1)
					S	0.3561(9)	0.25	0.017(1)	1	0.038(3)
$Sn_{0.81}S_{0.8}Se_{0.2}$		11.3096(5)	4.029(1)	4.352(1)	Sn	0.120(3)	0.25	0.112(6)	0.814(7)	0.017(1)
					S/Se	0.3576(9)	0.25	0.0167(9)	0.8/0.2	0.016(3)
$Sn_{0.81}Se$		11.5151(7)	4.1579(9)	4.4328(9)	Sn	0.1204(4)	0.25	0.099(1)	0.81(5)	0.016(1)
					Se	0.3561(5)	0.25	0.019(1)	1	0.020(3)

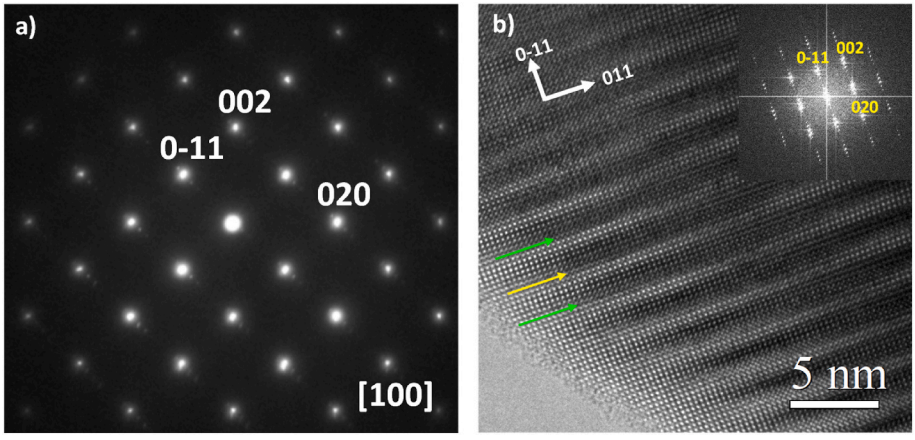

Fig. 2. (a) SAED pattern of $SnS_{0.8}Se_{0.2}$ crystal along the [100] zone axis. (b) HRTEM image of $SnS_{0.8}Se_{0.2}$ crystal along the [100] zone axis. The FFT in the inset shows extra spots observed along 0–11 confirming the modulation of the structure.

hexamethylenetetramine as an efficient precipitating agent for the formation of ZnO nanostructures was previously reported by Zhou et al. [43] and Wahab et al. [44]. The autoclave was introduced into the Milestone ETHOS 1 microwave and heated for 5 min at 100 °C. When the process was completed, the system was cooled naturally to room temperature. After that, the white polycrystalline product formed in the

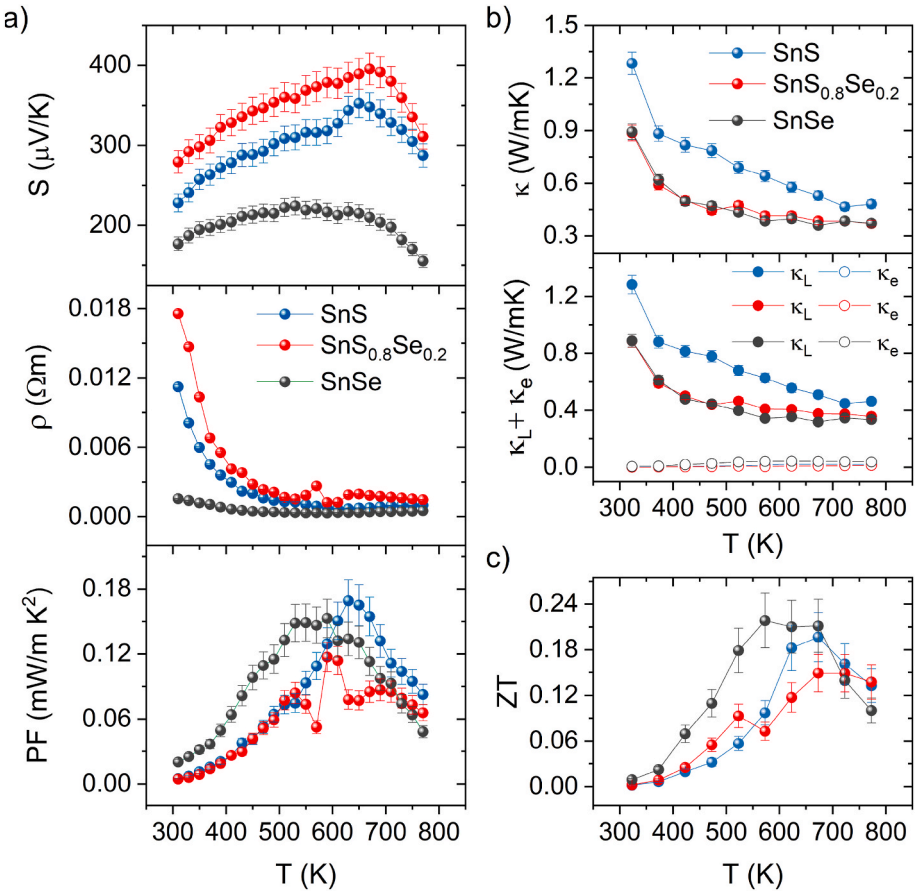

Fig. 3. Thermoelectric properties of $SnS_{1-x}Se_x$ (x = 0, 0.2, 1). Temperature dependence of (a) Seebeck coefficient, electrical resistivity and power factor (PF), (b) Total thermal conductivity, lattice and electronic contributions of the thermal conductivity, (c) figure of merit (zT).

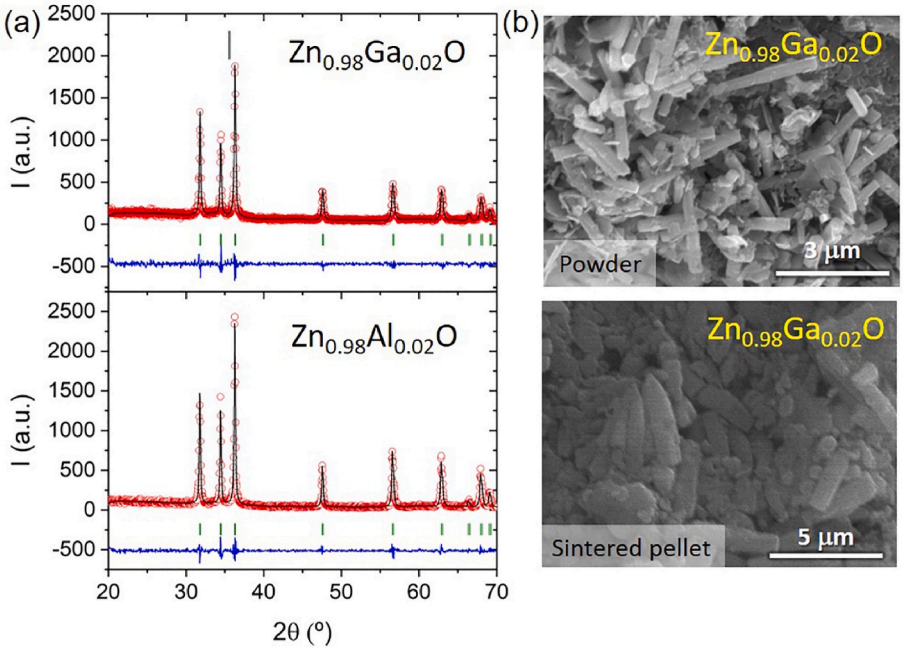

Fig. 4. (a) X-ray diffraction patterns at room temperature of microwave-synthesized $Zn_{0.98}M_{0.02}O$ (M = Al, Ga), refined in hexagonal *P6₃mc* space group: Observed (red circles), calculated (black line) and difference (blue line) profiles. Bragg positions are indicated as green vertical lines. (b) SEM micrographs of $Zn_{0.98}Ga_{0.02}O$ (powder and sintered). (For interpretation of the references to colour in this figure legend, the reader is referred to the Web version of this article.)

Table 2
Refined structural parameters obtained from powder X-ray diffraction for $Zn_{0.98}M_{0.02}O$ (M = Al, Ga) at room temperature (*P6₃mc* space group). (Refinement agreement factors: R_{Bragg} $Zn_{0.98}Al_{0.02}O$ = 2.21%; R_{Bragg} $Zn_{0.98}Ga_{0.02}O$ = 2.46%).

	Space Group	$a = b$/Å	c/Å	Atom	x	y	z	Occ	U_{iso}/Å^2
$Zn_{0.98}Al_{0.02}O$	***P6₃mc***	3.2514(2)	5.2069(4)	Zn/Al	0.333	0.666	0	0.98(1)/0.02(1)	0.008(4)
				O	0.333	0.666	0.381(1)	1	0.006(4)
$Zn_{0.98}Ga_{0.02}O$		3.2492(9)	5.2041(9)	Zn/Ga	0.333	0.666	0	0.98(1)/0.02(1)	0.007(4)
				O	0.333	0.666	0.380(1)	1	0.006(4)

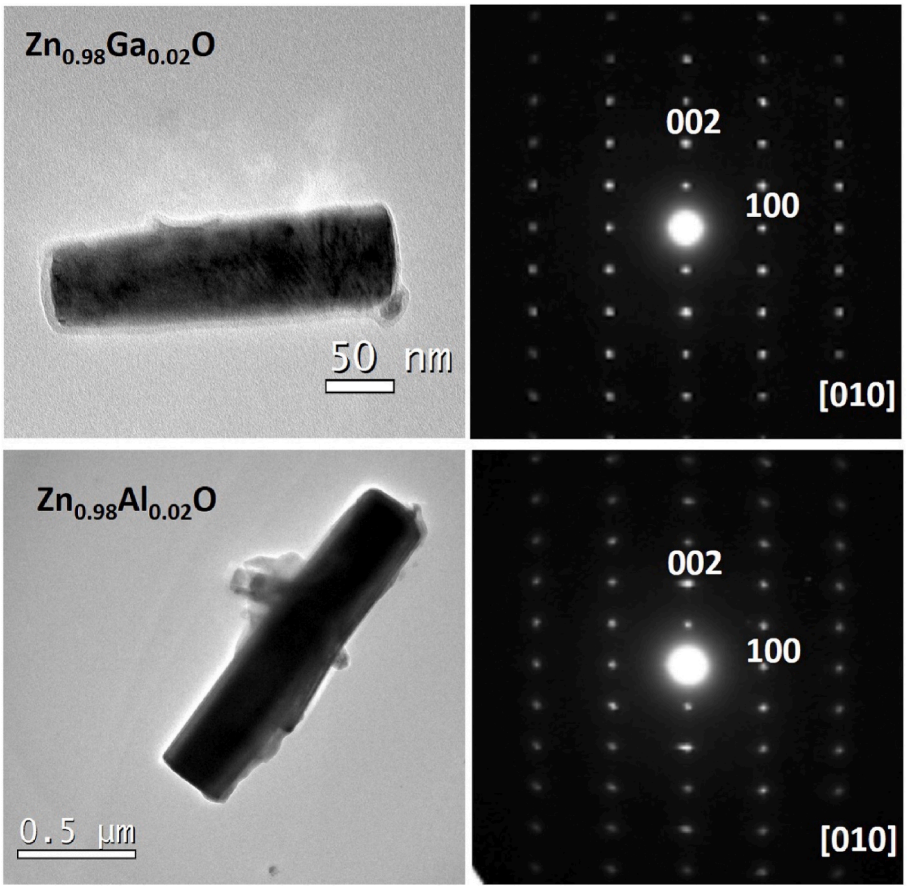

Fig. 5. TEM images and SAED patterns of $Zn_{0.98}M_{0.02}O$ (M = Al, Ga) crystals along the [010] zone axis.

microwave-coprecipitation process (≈0.6 g) was washed with distilled water and dried in an oven at 80 °C for 5 h.

2.1.3. Preparation of $Sr_{1-x}La_xTiO_{3-\delta}$ (x = 0, 0.05, 0.1) by microwave-combustion synthesis

Combustion is a versatile method for producing polycrystalline materials, principally oxides. The process involves an exothermic reaction between oxidizers precursors (*i.e.* metal nitrates) and a fuel (*i.e.* glycine, urea, sucrose, glucose, citric acid …), which are homogeneously mixed in an aqueous solution and heated in a hot-plate, in a furnace at mild conditions (200–500 °C) or in a microwave oven (as in this work). There are at least three thermodynamic processes during the synthesis: (a) heat generation, (b) gas expulsion (a fuel that decomposes in H_2O, CO_2 and N_2 non-toxic gases is employed) and (c) powder formation or crystallization. Occasionally, the desired product can be generated directly in the combustion, but usually a calcination step is necessary to remove organic waste and enhance crystallinity [45].

$Sr_{1-x}La_xTiO_{3-\delta}$ (x = 0, 0.05, 0.1) samples were synthesized by a microwave-combustion route. Stoichiometric amounts of $Sr(NO_3)_2$ (Alfa Aesar, 99.9%), $La(NO_3)_3.6H_2O$ (Sigma-Aldrich >99.99%) and TiO_2 (anatase, Sigma-Aldrich, 99.7%) – for the preparation of 5 mmol of product - were dissolved in a minimum amount of water and mixed with a glycine solution (in a 2:1 proportion with the total amount of precursor moles) in a porcelain capsule. The capsule was situated in the domestic microwave (ProClean 3010, Cedotec, 700 W) and after ca. 8 min of microwave radiation, the combustion occurs producing a greyish-powder. A calcination of ≈0.5 g of the product at 800 °C for 2 h was carried out to crystallize the phase and eliminate the organic remains.

2.1.4. Sintering by spark plasma sintering (SPS)

All the synthesized powders were sintered by using the SPS process. This is an advanced sintering technique that allows the compaction of the polycrystalline powder in short time (minutes) heating with an alternating current (AC) and, at the same time, applying uniaxial pressure. Similar to microwaves, SPS heating is internal, which facilitates an extremely rapid heating or cooling (up to 1000 °C/min). The explanation of the heating mechanism by SPS is controversial, but it is believed that Joule heating that comes from the graphite die and graphite foil plays a dominant role. There are other possible contributions: the direct current (DC) component included in pulse current, the skin effect of AC,

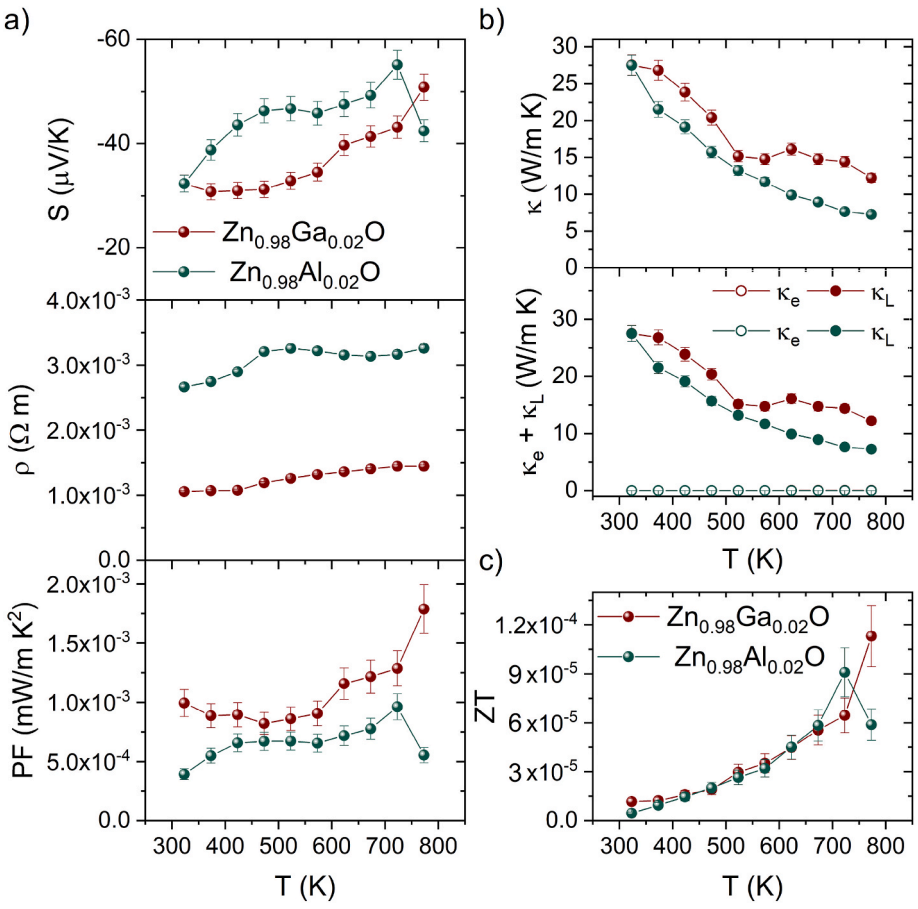

Fig. 6. Thermoelectric properties of $Zn_{0.98}M_{0.02}O$ (M = Al, Ga). Temperature dependence of (a) Seebeck coefficient, electrical resistivity and power factor (PF), (b) Total thermal conductivity, lattice and electronic contributions of the thermal conductivity, (c) figure of merit (zT).

the small heat capacity of the heated system or the heat effect of eddy current in grains (the latter contribution has an influence only for conductive materials) [46]. In the SPS process, the bulk is exposed to minimal thermal effects. As a result, the microstructure of the powder is conserved and there is not a significant particle growth.

A DR. SINTER LAB Jr. sps-212Lx SPS instrument was used for the sintering of the materials described in this work. Synthesized powder was introduced in an 8 mm diameter graphite die and wrapped with graphite foil. Uniaxial pressure was programmed to 50 MPa and the heating time was limited to 5 min. The process occurs under vacuum. Temperature was optimized for all the samples. In the case of SnS, SnSe and $SnS_{0.8}Se_{0.2}$ samples, a temperature of 450 °C is required, while 900 °C was used for $Zn_{0.98}M_{0.02}O$ (M = Al, Ga) and 1200 °C for $Sr_{1-x}La_xTiO_{3-\delta}$ *(x = 0, 0.05, 0.1)*. A graphite foil covers the inner part of the SPS graphite die. Once the process finishes, the pellet is ground and polished to remove any remnants of this foil. The estimation of the density of the pellets was done by measuring volume and weight of the pellet and all of them are in the range of ≈93–98% of their crystallographic densities [SnS (96%); $SnS_{0.8}Se_{0.2}$ (96%); SnSe (98%); $Zn_{0.98}Al_{0.02}O$ (93%); $Zn_{0.98}Ga_{0.02}O$ (92%); $Sr_{0.95}La_{0.05}TiO_{3-\delta}$ (95%); $Sr_{0.9}La_{0.1}TiO_{3-\delta}$ (94%)].

2.2. Characterization

2.2.1. Structural and microstructural characterization

Room temperature X-ray diffraction (*Cu*-Kα radiation) was performed on an X'Pert MPD PANalytical Instrument diffractometer. The 2θ range for the measurement was $10° < 2\theta < 70°$ with step size $\Delta(2\theta) = 0.02°$. Rietveld refinements from X-ray diffraction patterns of the powders were carried out by using FullProf software [47]. The diffraction pattern reflections were fitted by a pseudo-Voigt function. Scale factor, background, zero-shift, asymmetry, lattice parameters, atomic positions, occupancy and displacement parameters were refined. The refinements have been done considering isotropic vibrations, which means that atoms vibrate in all directions equally.

Scanning electron microscopy (SEM) of gold-coated powders was carried out using a JEOL 6400 microscope equipped with a detector for energy-dispersive analysis of X-rays (EDAX), while a JEOL 3000F microscope was used for high resolution transmission electron microscopy (HRTEM) and selected-area electron diffraction (SAED). Fast Fourier transforms (FFTs) of the HRTEM images were carried out using Gatan Microscopy Suite Software.

2.2.2. Thermoelectric properties

Thermoelectric characterization of the materials is done in consistent pellets prepared by SPS. For that, a thin slide of the pellet (≈ 0.3 mm) is cut with a diamond saw and reserved for thermal diffusivity measurements, while a bar-shaped part is also cut for Seebeck coefficient measurements. Electrical resistivity is determined in the remaining part of the pellet.

A commercial MMR-technologies system was used for the determination of the Seebeck coefficient of the samples. Measurements were performed under vacuum conditions (10^{-3} mbar) from 300 to 800 K. A reference (constantan wire) was measured for comparison with bar-shaped samples, previously cut with a diamond saw perpendicular to the pressing direction. Electrical resistivity was measured in the same instrument using van der Pauw method.

Thermal diffusivity (α) was measured in a Linseis LFA 1000 instrument from 300 to 800 K under Argon. A thin graphite coating was

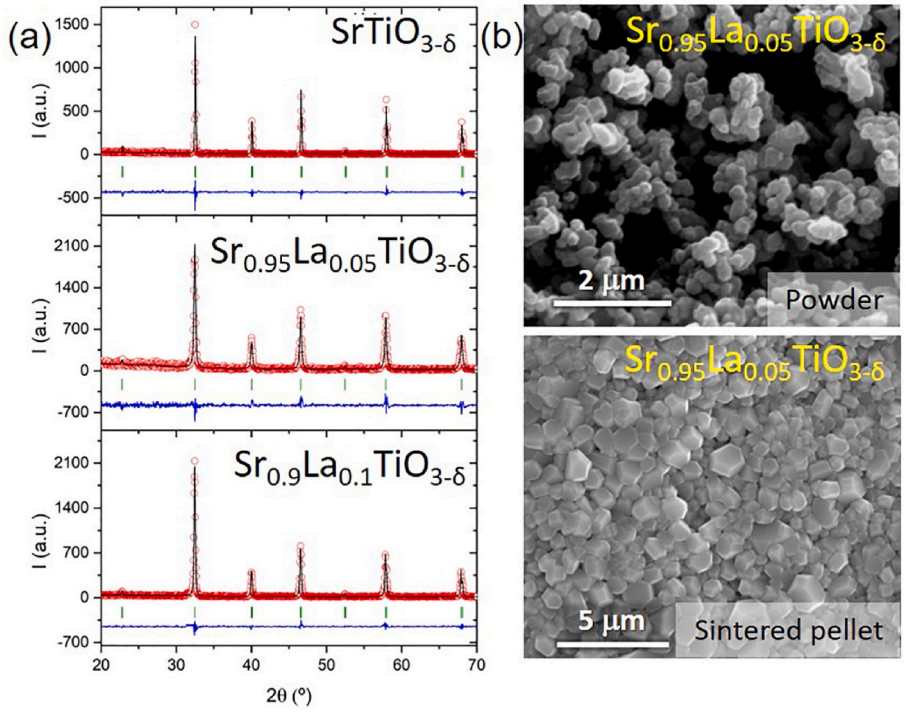

Fig. 7. (a) X-ray diffraction patterns at room temperature of microwave-synthesized $Sr_{1-x}La_xTiO_{3-\delta}$ (x = 0, 0.05, 0.1), refined in cubic *Pm-3m* space group: Observed (red circles), calculated (black line) and difference (blue line) profiles. Bragg positions are indicated as green vertical lines. (b) SEM micrographs of $Sr_{0.95}La_{0.05}TiO_{3-\delta}$ (powder and sintered). (For interpretation of the references to colour in this figure legend, the reader is referred to the Web version of this article.)

Table 3
(a) Refined structural parameters obtained from powder X-ray diffraction for $Sr_{1-x}La_xTiO_{3-\delta}$ (x = 0, 0.05, 0.1) at room temperature (Pm-3m space group). (Refinement agreement factors: R_{Bragg} $SrTiO_3$ = 2.36%; R_{Bragg} $Sr_{0.95}La_{0.05}TiO_{3-\delta}$ = 3.65%; R_{Bragg} $Sr_{0.9}La_{0.1}TiO_{3-\delta}$ = 2.97%).

	Space Group	$a = b = c$/Å	Atom	x	y	z	Occ	U_{iso}/Å^2
$SrTiO_3$	***Pm-3m***	3.8954(3)	Sr	0	0	0	1	0.005(1)
			Ti	0.5	0.5	0.5	1	0.003(1)
			O	0	0.5	0.5	1	0.01
$Sr_{0.95}La_{0.05}TiO_{3-\delta}$		3.8985(5)	Sr/La	0	0	0	0.95(2)/0.05(1)	0.006(1)
			Ti	0.5	0.5	0.5	1	0.002(2)
			O	0	0.5	0.5	1	0.01
$Sr_{0.9}La_{0.1}TiO_{3-\delta}$		3.9014(3)	Sr/La	0	0	0	0.89(1)/0.11(1)	0.005(1)
			Ti	0.5	0.5	0.5	1	0.002(1)
			O	0	0.5	0.5	1	0.01

deposited on the surface of pellets to increase the heat absorption and emissivity. Samples were measured along the SPS direction. The thermal conductivity (κ) was calculated by using the expression $\kappa = \alpha \cdot C_p \cdot d$, where C_p corresponds to the specific heat and d is the sample density. Specific heat was estimated by Dulong–Petit law [48].

3. Results and discussion

3.1. Tin chalcogenides

Fig. 1a displays the Rietveld refinement analyses of the powder X-ray diffraction patterns for SnS, $SnS_{0.8}Se_{0.2}$ and SnSe. The three phases were refined in the orthorhombic *Pnma* space group. Unit cell parameters, atomic positions, occupancy and displacement parameters are summarized in Table 1. The results of the Rietveld refinements confirm that the preparation of these materials by means of microwave-hydrothermal synthesis produces the formation of Sn vacancies ($Sn_{0.835(7)}S$, $Sn_{0.814(7)}S_{0.8}Se_{0.2}$, $Sn_{0.81(5)}Se$), randomly located in the structure. The existence of these vacancies would have a noteworthy effect in the thermoelectric properties, as the carrier concentration of the materials is modified. Yang et al. [23] demonstrated that stoichiometric SnS sample possesses a low hole concentration of 10^{16} cm^{-3} at room temperature, while an increment to 10^{19} cm^{-3} is produced when preparing $Sn_{0.85}S$ by a cationic lattice site vacancy engineering strategy.

SEM micrographs of the powder show an agglomeration of particles with a considerable porosity (Fig. 1b). The relatively uniform size and shape of the particles facilitate the sintering by SPS. A semi-quantitative EDAX study in 10 points of the powders is in good agreement with the compositional results extracted from the Rietveld refinements.

Further insight into the structure of the synthesized phases was acquired from transmission electron microscopy (TEM). The samples exhibit good crystallinity despite the short processing time. The study of the reciprocal space by selected area electron diffraction (SAED), confirms the orthorhombic structure for the three chalcogenides, however in some crystals the patterns recorded along the [100] zone axes apart from the strong basic reflections, an additional weak diffraction maximum is observed, which are incommensurate with the basic lattice (Fig. 2a). The satellite reflections are characterized by a modulation vector q = 0.13xd(0–11) and have not been previously reported in these types of chalcogenides. The HRTEM images of modulated crystals along the [100] zone axis are similar to the one displayed in Fig. 2b, which corresponds to $SnS_{0.8}Se_{0.2}$. The contrast of the micrograph reveals that

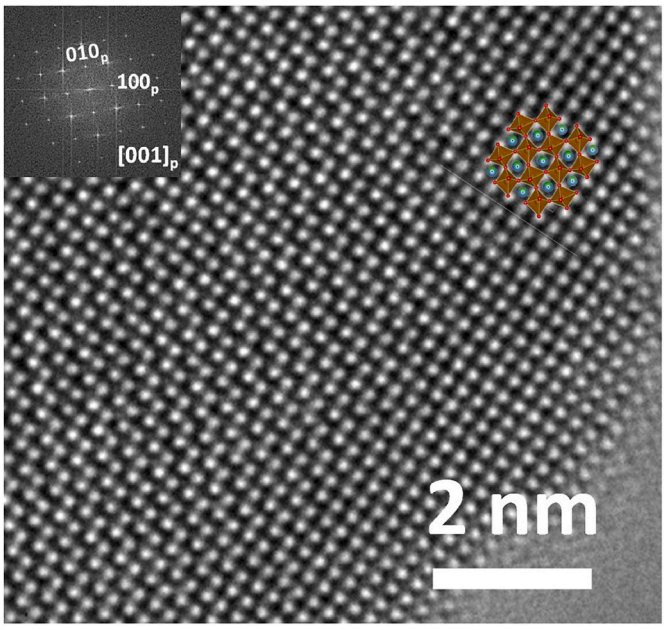

Fig. 8. HRTEM image of $Sr_{0.95}La_{0.05}TiO_{3-\delta}$ crystal along the [001] zone axis. The FFT in the inset does not show any extra spot or streaking. Crystal model is shown on top of the HRTEM image: green balls correspond to La/Sr atoms, red balls indicate oxygen positions, while brownish octahedra are formed by TiO_6. (For interpretation of the references to colour in this figure legend, the reader is referred to the Web version of this article.)

the origin of the modulation is the formation of blocks with a thickness of ~7.5xd(0–11) with a ½ shift along the (011) direction (marked with the yellow arrow in the image), yielding a centered superstructure with a size ~15xd(0–11) (marked with the green arrows in the HRTEM image).

Thermoelectric properties of SnS, $SnS_{0.8}Se_{0.2}$ and SnSe as a function of temperature and measured along the perpendicular of the pressing direction are summarized in Fig. 3. The positive value of the Seebeck coefficient (S) (top panel of Fig. 3a) indicates the p-type semiconductor character of the compounds along the studied temperature range. The maximum Seebeck coefficient was found for SnS0.8Se0.2 sample, with a value that is increased from 280 μV K^{-1} at room temperature to 393 μV K^{-1} at 673 K. At higher temperatures, a reduction of S is noticeable, which is attributed to the bipolar effect [49]. The same behaviour was found for SnS and SnSe. Seebeck coefficient values are comparable to previously reported for $SnS_{1-x}Se_x$ materials produced by other synthetic techniques, such as ball milling [50], hydrothermal [49,51] or melting-annealing process [20].

Electrical resistivity (middle panel of Fig. 3a) decreases when heating the samples. However, in the three samples, at ca. 500 K there is a plateau with a slight increase of electrical resistivity at higher temperatures. This behaviour was previously described for SnSe and points to the phonon scattering mechanism as the dominant factor of the electronic resistivity at high temperatures, whereas the grain boundary potential barrier affects the mobility of the charge carrier at the lower temperature regime [51]. SnSe presents the lowest electrical resistivity value (1.5×10^{-3} Ω·m at room temperature and 3.0×10^{-4} Ω·m at 590 K), although over 550 K there is no significant difference in SnSe and SnS values (electrical resistivity of SnS at 590 K: 7.8×10^{-4} Ω·m). As a result, the maximum of the power factor ($PF = S^2/\rho$) of SnSe and SnS are close:

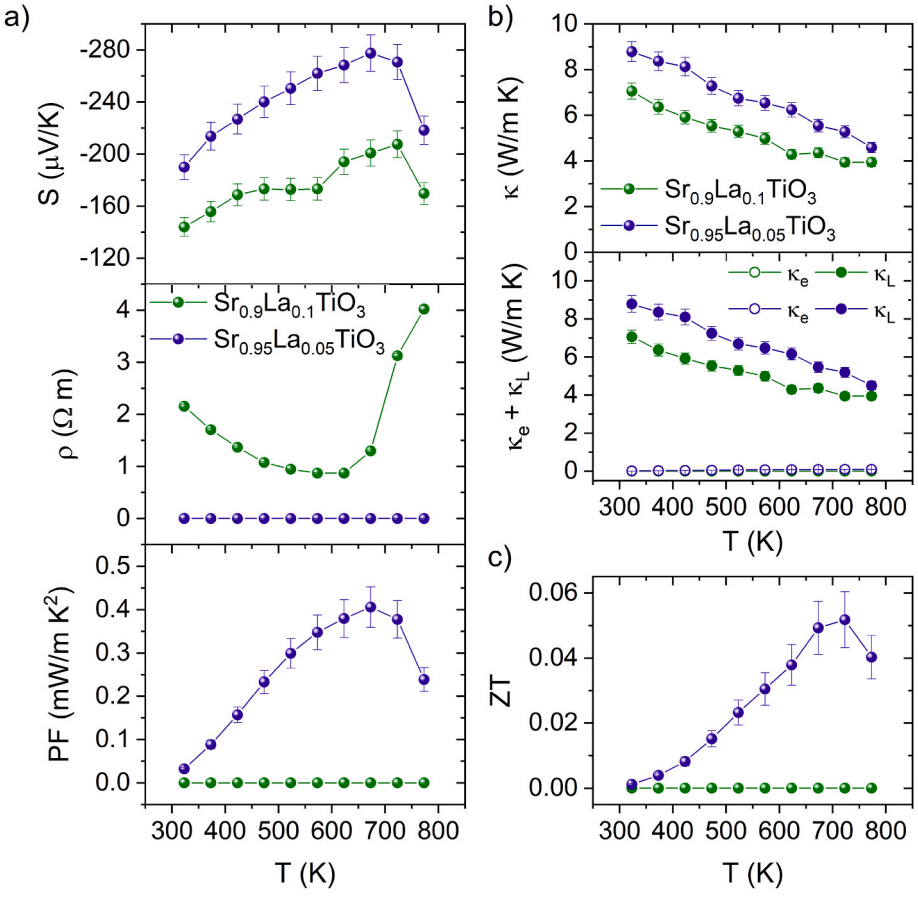

Fig. 9. Thermoelectric properties of $Sr_{1-x}La_xTiO_{3-\delta}$ (x = 0.05, 0.1). Temperature dependence of (a) Seebeck coefficient, electrical resistivity and power factor (PF), (b) Total thermal conductivity, lattice and electronic contributions of the thermal conductivity, (c) figure of merit (zT).

0.17 mW/m·K^2 at 630 K for SnSe and 0.15 mW/m·K^2 at 590 K for SnS.

Fig. 3b shows the temperature dependence of the thermal conductivity. A decrease of κ is observed when heating the samples. Although the total thermal conductivity is relatively low for the three samples, κ of SnS is ca. 30% higher than κ of $SnS_{0.8}Se_{0.2}$ and SnSe at room temperature. The minimum κ value was found for SnSe (0.36 W/m·K at 673 K), as it can be observed in the bottom panel of Fig. 3b. It is associated with the relatively high electrical resistivity of the samples, the total thermal conductivity is mainly controlled by the lattice thermal conductivity (κ_L) and the electrical thermal conductivity (κ_e) has a minimum influence. The low thermal conductivity achieved for these phases is attributed to the intrinsic giant anharmonicity due to the layered structure and anisotropic bonding together with the weak cross-layer interatomic interactions and the reduced phonon group velocity [52]. The thermal conductivity decreases following $\kappa = \alpha \cdot T^{-1}$ equation. This trend is observed when the phonon scattering is dominated by Umklapp processes [53].

Taking into account the electrical and thermal properties of the materials, the dimensionless figure of merit zT was determined and represented in Fig. 3c. A maximum value of 0.22 at 573 K was found for SnSe, while SnS presents a comparable figure of merit $zT = 0.20$ at 673 K. The thermoelectric performance is not ideal for technological application since $zT < 1$. However, the thermoelectric results found for these systems are similar to other works published for undoped tin chalcogenides [22,54,55]. Adequate doping may improve the efficiency of these systems as it is shown in Asfandiyar et al. work, where the figure of merit was increased from $zT = 0.2$ at 877 K for SnS to $zT = 1.1$ at the same temperature by doping with Ag [55].

3.2. $Zn_{0.98}M_{0.02}O$ (M = Al, Ga)

Phase purity and wurtzite-type structure (hexagonal phase, $P6_3mc$ space group) were confirmed from the powder X-ray diffraction patterns and Rietveld refinements of $Zn_{0.98}M_{0.02}O$ (M = Al, Ga) (Fig. 4a). Unit-cell parameters, atomic positions, occupancy and displacement parameters are summarized in Table 2. The structural information obtained after Rietveld refinement is in good agreement with data reported in the literature [56,57]. Although ZnO possesses low solubility limits for doping, based on the X-ray diffraction results and EDAX analysis, we can confirm that Al and Ga are part of the structure. An increment of the doping level would produce the appearance of secondary phases: $ZnAl_2O_4$ or $Zn_9Ga_2O_{12}$, when % of Al or Ga are >2% [57]. As an example, SEM micrographs of $Zn_{0.98}Ga_{0.02}O$ (powder and sintered) are shown in Fig. 4b. The particles of $Zn_{0.98}Al_{0.02}O$ and $Zn_{0.98}Ga_{0.02}O$ synthesized by microwave-coprecipitation route crystallize in homogenous rod-shape form (Figs. 4b and 5).

The structure of the individual $Zn_{0.98}M_{0.02}O$ (M = Al, Ga) rods was further characterized by TEM and SAED (Fig. 5). Isolated rods were identified for both compositions. SAED patterns taken along the [010] zone axes are in good agreement with the wurtzite structure observed by X-ray diffraction for both oxides. The absence of extra reflections, streaking lines or scattering diffuse between the basic reflections confirms the absence of extended defects in the rods.

Fig. 6 represents the thermoelectric properties of $Zn_{0.98}M_{0.02}O$ (M = Al, Ga). Seebeck coefficient is negative for the two materials in the measured temperature range, indicating an n-type semiconducting character (top panel - Fig. 6a), i.e. the negative free charges will produce a negative potential at the cold end of the thermoelectric device. This kind of conductivity was previously described for bulk ZnO. Although undoped ZnO presents a wide band gap between 3.2 and 3.5 eV [58], doping with small amounts of elements, such as Al or Ga, produces an increment of the electrical conductivity changing the conduction to a more metallic scenario. In this case, it can be observed that the electrical resistivity is slightly higher for $Zn_{0.98}Al_{0.02}O$ (ρ = 2.66 x 10-3 Ω·m at room temperature) than for $Zn_{0.98}Ga_{0.02}O$ (ρ = 1.05 x 10-3 Ω·m at room temperature). Although the electrical resistivity values are appropriate for thermoelectric applications (middle panel – Fig. 6a), the relatively low Seebeck coefficient produces a low power factor too (bottom panel - Fig. 6a). Thermal conductivity of the two materials is quite large at room temperature (≈30 W/m·K in both cases), but there is a constant decrease of κ when heating (≈12 W/m·K and 7 W/m·K at 773 K for $Zn_{0.98}Al_{0.02}O$ and $Zn_{0.98}Ga_{0.02}O$, respectively). These findings are consistent to that reported by Mele et al. [59] although, in their work, Seebeck coefficient values were higher. Total thermal conductivity is principally controlled by the lattice thermal conductivity. The thermal conductivity curve found for these two samples is similar to the one described for other oxides in the temperature range over which resistive phonon–phonon interactions (Umklapp processes) are the main scattering mechanism [60]. Overall, both compositions present the same temperature dependence of the figure of merit zT (Fig. 6c) but achieving zT values (in the described temperature range) far from commercial thermoelectric materials.

3.3. $Sr_{1-x}La_xTiO_{3-\delta}$ (x = 0, 0.05, 0.1)

Rietveld refinements of the X-ray diffraction patterns for $Sr_{1-x}La_xTiO_{3-\delta}$ (x = 0, 0.05, 0.1) confirm the cubic symmetry and *Pm-3m* space group (Fig. 7a). Table 3 shows the unit cell parameters, atomic positions, occupancy and displacement parameters of the three compositions. As a result of the larger size of La compared to Sr, there is an increment in the unit cell dimensions for the La-containing samples. $Sr_{1-x}La_xTiO_{3-\delta}$ compounds are oxygen-deficient ceramics, which dramatically affect the charge-carrier concentration (electronic properties) and thermal properties of the phases [61]. In order to quantify the oxygen vacancies, neutron diffraction experiments would be necessary [33]. As an example, Fig. 7b reveals representative SEM images of the powder and the cross section of a sintered pellet of $Sr_{0.95}La_{0.05}TiO_{3-\delta}$. A uniform grain structure and grain size distribution is evident.

HRTEM microstructure study of $Sr_{0.95}La_{0.05}TiO_{3-\delta}$ along the main zone axis [001] is shown in Fig. 8. The sample is homogenous and the crystal structure is well ordered, with no presence of additional reflections or streaking visible in the FFT inset of the image, suggesting the absence of cation or vacancy ordering. The direct measurement of a and b parameters in the image gives a value of 3.9 Å, consistent with the unit cell size determined by X-ray diffraction. On the HRTEM image, a representation of the structure is indicated, showing TiO_6 octahedra coloured in brown and Sr/La cations in green, which match perfectly with the different contrasts of the micrograph.

$Sr_{1-x}La_xTiO_{3-\delta}$ (x = 0.05, 0.1) phases have been considered potential thermoelectric materials at high temperatures. Computational predictions indicate that zT ≈ 0.7 may be reached at 1400 K for La-doped $SrTiO_3$ [62]. This high temperature is outside our measurement range, but it gives an idea about the possibilities of these oxides for high-temperature applications. Doping $SrTiO_3$ with La^{3+} creates a defective structure, enclosing O-site vacancies with mixed Ti^{3+} and Ti^{4+} in the B position of the perovskite. As a result, electronic properties are tuned to a more conductive scenario. Due to the insulator character of $SrTiO_3$ (wide band gap of ≈3.2 eV with a low charge carrier concentration), electronic properties could not be determined by our MMR-technologies system and other techniques, such as impedance spectroscopy, are necessary to study the electronic properties of the sample. Furthermore, previous reports indicate that the thermal conductivity of the pristine $SrTiO_3$ sample is large for thermoelectric applications (9–12 W/m·K) [33,34,63]. However, when doping with La^{3+}, the Fermi level is raised from the forbidden band to the conduction band, as electrons have been incorporated. As a result, phonon-electron coupling occurs and it drives the formation of polarons [63].

Fig. 9 shows the thermoelectric properties found for $Sr_{1-x}La_xTiO_{3-\delta}$ (x = 0.05, 0.1) from 300 to 800 K. Seebeck coefficient is negative for both samples, indicating n-type conduction (upper panel Fig. 9a). It is observed a higher value (in absolute terms) for $Sr_{0.95}La_{0.05}TiO_{3-\delta}$. In this sample a maximum Seebeck coefficient of −277 μV/K was measured at

690 K. This is ≈ 27% higher than the value found for $Sr_{0.9}La_{0.1}TiO_{3-\delta}$. In the middle panel of Fig. 9a, it can be observed that the electrical resistivity of $Sr_{0.9}La_{0.1}TiO_{3-\delta}$ ($\rho \approx 2$ Ω·m at room temperature, 0.9 Ω·m at 773 K) is much higher than for the sample $Sr_{0.95}La_{0.05}TiO_{3-\delta}$ ($\rho \approx 1.1$ x 10-3 Ω·m at room temperature, 1.9 x 10-4 Ω·m at 773 K). As a result, the maximum power factor was achieved for $Sr_{0.95}La_{0.05}TiO_{3-\delta}$ (PF ≈ 0.4 at $mW/m{\cdot}K^2$ at 673 K). Concerning the thermal properties of these compositions (Fig. 9b), a clear reduction of κ when heating is visible. Although the room temperature values are considerably high for thermoelectric applications (κ ≈ 8.8 W/m·K and 7.1 W/m·K for $Sr_{0.95}La_{0.05}TiO_{3-\delta}$ and $Sr_{0.9}La_{0.1}TiO_{3-\delta}$, respectively), the possible utilization of these materials at higher temperatures are confirmed by the decrease of κ when heating (κ ≈ 4.5 W/m·K and 3.9 W/m·K for $Sr_{0.95}La_{0.05}TiO_{3-\delta}$ and $Sr_{0.9}La_{0.1}TiO_{3-\delta}$ at 773 K, respectively). Again, total thermal conductivity is predominantly attributed to the lattice thermal conductivity.

The combination of the electrical and thermal properties results in the figures of merit represented in Fig. 9c. A maximum zT of ≈0.05 at 723 K is achieved for $Sr_{0.95}La_{0.05}TiO_{3-\delta}$ (Fig. 9c). These values may be improved at higher temperatures. Even though zT values are distant from commercial thermoelectric compounds, the results shown here suggest that further control of doping, vacancies concentration and the utilization of new synthetic routes can be encouraging strategies for the optimization of the thermoelectric properties in oxides.

4. Conclusions

In conclusion, microwave-chemistry is a powerful tool for the synthesis of oxide and chalcogenide thermoelectrics. In this work, we show the microwave-preparation, the structural and thermoelectric properties of $SnS_{1-x}Se_x$ (x = 0, 0.2, 1), $Zn_{0.98}M_{0.02}O$ (M = Al, Ga) and $Sr_{1-x}La_xTiO_{3-\delta}$ (x = 0, 0.05, 0.1).

(a) $SnS_{1-x}Se_x$ (x = 0, 0.2, 1) phases were synthesized by microwave-hydrothermal in just 1-min. The materials exhibit an orthorhombic *Pnma* space group at room temperature and Rietveld refinement confirms the existence of tin vacancies in the three prepared phases. A localized structural modulation was found in the HRTEM study. Thermoelectric efficiency is similar for isoelectronic SnS and SnSe ($zT = 0.22$ at 573 K for SnSe and $zT = 0.20$ at 673 K for SnS).

(b) $Zn_{0.98}M_{0.02}O$ (M = Al, Ga) rods were synthesized by microwave-coprecipitation route in 5 min. Both materials show a wurtzite-type structure (*P6₃mc* space group confirmed by Rietveld refinements). Thermoelectric properties reveal an n-type conducting behavior. Although, Al-doped sample is slightly more resistive than Ga-doped ZnO, thermal conductivity is lower and as a result, zT values are very similar for the two compounds.

(c) $Sr_{1-x}La_xTiO_{3-\delta}$ (x = 0, 0.05, 0.1) powders were synthesized by microwave-combustion route. The combustion occurs after 8 min of microwave irradiation. The samples are cubic *Pm-3m*. HRTEM micrograph shows a well-ordered crystal structure and defects are not observed. Thermoelectric properties of these n-type materials show that the maximum thermoelectric performance is found for $Sr_{0.95}La_{0.05}TiO_{3-\delta}$ composition.

Further optimization of the doping level of the synthesized materials is required in order to achieve competitive thermoelectric performance.

Acknowledgments

The authors are gratefully indebted to Community of Madrid for the concession of the project PR65/19-22459 under the Multiannual Agreement with Complutense University in the line Program to Stimulate Research for Young Doctors in the context of the V PRICIT (Regional Programme of Research and Technological Innovation). Furthermore, this research publication is also part of the projects PID2020-112848RB-C21 and MAT2017-84496-R founded by MCIN/AEI/10.13039/501100011033. JPG and MMGB would also like to thank Community of Madrid for the concession of PEJ-2020-AI/IND-17706 research assistant contract, through the Youth Employment Operational Program and the Youth Employment Initiative, while V.C. thanks the Community of Madrid for for granting the "Atracción de Talento program" fellowship, 2019-T2/IND-13483.

We wish to express our gratitude to CNME and X-ray diffraction (UCM CAI) technical staff for making the facilities available for the structural characterization of the materials. We are indebted to I. Aguayo, S. Rodríguez, J. González-Cassy and E. de Areba for help and support.

References

[1] J.D. Sachs, G. Schmidt-Traub, J. Williams, Pathways to zero emissions, Nat. Geosci. 9 (2016) 799–801.
[2] J.M. Chen, Carbon neutrality: toward a sustainable future, Innovation 2 (2021) 100127.
[3] T.J. Seebeck, Magnetische polarisation der metalle und erze durch temperatur-differenz, Abhandlungen der Königlichen Akademie der Wissenschaften zu Berlin, Königliche Akademie der Wissenschaften, 1825, pp. 289–346.
[4] L.E. Bell, Cooling, heating, generating power, and recovering waste heat with thermoelectric systems, Science 321 (2008) 1457–1461.
[5] G.J. Snyder, E.S. Toberer, Complex thermoelectric materials, Nat. Mater. 7 (2008) 105–114.
[6] C. Forman, I.K. Muritala, R. Pardemann, B. Meyer, Estimating the global waste heat potential, Renew. Sustain. Energy Rev. 57 (2016) 1568–1579.
[7] H. Alam, S. Ramakrishna, A review on the enhancement of figure of merit from bulk to nano-thermoelectric materials, Nano Energy 2 (2013) 190–212.
[8] T.M. Tritt, M. Subramanian, Thermoelectric materials, phenomena, and applications: a bird's eye view, MRS Bull. 31 (2006) 188–198.
[9] J. Prado-Gonjal, M. Phillips, P. Vaqueiro, G. Min, A.V. Powell, Skutterudite thermoelectric modules with high volume-power-density: scalability and reproducibility, ACS Appl. Energy Mater. 1 (2018) 6609–6618.
[10] J. Gainza, F. Serrano-Sánchez, J.E. Rodrigues, J. Prado-Gonjal, N.M. Nemes, N. Biskup, O.J. Dura, J.L. Martínez, F. Fauth, J.A. Alonso, Unveiling the correlation between the crystalline structure of M-filled $CoSb_3$ (M= Y, K, Sr) Skutterudites and their thermoelectric transport properties, Adv. Funct. Mater. 30 (2020) 2001651.
[11] M. Rull-Bravo, A. Moure, J. Fernández, M. Martín-González, Skutterudites as thermoelectric materials: revisited, RSC Adv. 5 (2015) 41653–41667.
[12] C. Fu, S. Bai, Y. Liu, Y. Tang, L. Chen, X. Zhao, T. Zhu, Realizing high figure of merit in heavy-band p-type half-Heusler thermoelectric materials, Nat. Commun. 6 (2015) 1–7.
[13] K. Xia, C. Hu, C. Fu, X. Zhao, T. Zhu, Half-Heusler thermoelectric materials, Appl. Phys. Lett. 118 (2021) 140503.
[14] A. Nozariasbmarz, A. Agarwal, Z.A. Coutant, M.J. Hall, J. Liu, R. Liu, A. Malhotra, P. Norouzzadeh, M.C. Oeztuerk, V.P. Ramesh, Thermoelectric silicides: a review, Jpn. J. Appl. Phys. 56 (2017), 05DA04.
[15] H. Kleinke, New bulk materials for thermoelectric power generation: clathrates and complex antimonides, Chem. Mater. 22 (2010) 604–611.
[16] A.V. Powell, P. Vaqueiro, Chalcogenide Thermoelectric Materials, Thermoelectric Materials and Devices, 2016, p. 27. RSC.
[17] C. Han, Q. Sun, Z. Li, S.X. Dou, Thermoelectric enhancement of different kinds of metal chalcogenides, Adv. Energy Mater. 6 (2016) 1600498.
[18] R. Freer, A.V. Powell, Realising the potential of thermoelectric technology: a Roadmap, J. Mater. Chem. C 8 (2020) 441–463.
[19] L.-D. Zhao, S.-H. Lo, Y. Zhang, H. Sun, G. Tan, C. Uher, C. Wolverton, V.P. Dravid, M.G. Kanatzidis, Ultralow thermal conductivity and high thermoelectric figure of merit in SnSe crystals, Nature 508 (2014) 373–377.
[20] C. Zhou, Y.K. Lee, Y. Yu, S. Byun, Z.-Z. Luo, H. Lee, B. Ge, Y.-L. Lee, X. Chen, J. Y. Lee, Polycrystalline SnSe with a thermoelectric figure of merit greater than the single crystal, Nat. Mater. (2021) 1–7.
[21] J. Prado-Gonjal, J. Gainza, I. Aguayo, Ó.J. Durá, S. Rodríguez-Pérez, F. Serrano-Sánchez, N.M. Nemes, M.T. Fernández-Díaz, J.A. Alonso, E. Morán, High thermoelectric performance of rapidly microwave-synthesized $Sn_{1-\delta}S$, Mater. Adv. 1 (2020) 845–853.
[22] Z. Wang, D. Wang, Y. Qiu, J. He, L.-D. Zhao, Realizing high thermoelectric performance of polycrystalline SnS through optimizing carrier concentration and modifying band structure, J. Alloys Compd. 789 (2019) 485–492.

[23] H.Q. Yang, X.Y. Wang, H. Wu, B. Zhang, D.D. Xie, Y.J. Chen, X. Lu, X.D. Han, L. Miao, X.Y. Zhou, Sn vacancy engineering for enhancing the thermoelectric performance of two-dimensional SnS, J. Mater. Chem. C 7 (2019) 3351–3359.

[24] K. Koumoto, R. Funahashi, E. Guilmeau, Y. Miyazaki, A. Weidenkaff, Y. Wang, C. Wan, Thermoelectric ceramics for energy harvesting, J. Am. Ceram. Soc. 96 (2013) 1–23.

[25] J. He, Y. Liu, R. Funahashi, Oxide thermoelectrics: the challenges, progress, and outlook, J. Mater. Res. 26 (2011) 1762–1772.

[26] M. Ito, T. Nagira, D. Furumoto, S. Katsuyama, H. Nagai, Synthesis of $Na_xCo_2O_4$ thermoelectric oxides by the polymerized complex method, Scripta Mater. 48 (2003) 403–408.

[27] P. Liu, G. Chen, Y. Cui, H. Zhang, F. Xiao, L. Wang, H. Nakano, High temperature electrical conductivity and thermoelectric power of Na_xCoO_2, Solid State Ionics 179 (2008) 2308–2312.

[28] W. Zhang, K. Zhu, J. Liu, J. Wang, K. Yan, P. Liu, Y. Wang, Influence of the phase transformation in Na_xCoO_2 ceramics on thermoelectric properties, Ceram. Int. 44 (2018) 17251–17257.

[29] C. Kim, D. Kim, H. Hong, K. Park, Thermoelectric properties of La^{3+} and Ce^{3+} co-doped $CaMnO_3$ prepared by tape casting, J. Eur. Ceram. Soc. 40 (2020) 735–741.

[30] Y. Wang, Y. Sui, H. Fan, X. Wang, Y. Su, W. Su, X. Liu, High temperature thermoelectric response of electron-doped $CaMnO_3$, Chem. Mater. 21 (2009) 4653–4660.

[31] B. Zhu, C. Chen, Z. Yao, J. Chen, C. Jia, Z. Wang, R. Tian, L. Tao, F. Xue, H. Hng, Multiple doped ZnO with enhanced thermoelectric properties, J. Eur. Ceram. Soc. 41 (2021) 4182–4188.

[32] K. Cai, E. Müller, C. Drašar, A. Mrotzek, Preparation and thermoelectric properties of Al-doped ZnO ceramics, Mater. Sci. Eng., B 104 (2003) 45–48.

[33] J. Prado-Gonjal, C. López, R. Pinacca, F. Serrano-Sánchez, N. Nemes, O. Dura, J. Martínez, M. Fernández-Díaz, J. Alonso, Correlation between crystal structure and thermoelectric properties of $Sr_{1-x}Ti_{0.9}Nb_{0.1}O_{3-\delta}$ ceramics, Crystals 10 (2020) 100.

[34] S.R. Popuri, A. Scott, R. Downie, M. Hall, E. Suard, R. Decourt, M. Pollet, J.-W. Bos, Glass-like thermal conductivity in $SrTiO_3$ thermoelectrics induced by A-site vacancies, RSC Adv. 4 (2014) 33720–33723.

[35] H. Wang, W. Su, J. Liu, C. Wang, Recent development of n-type perovskite thermoelectrics, J. Mater. 2 (2016) 225–236.

[36] H. Wang, C. Wang, Thermoelectric properties of Yb-doped $La_{0.1}Sr_{0.9}TiO_3$ ceramics at high temperature, Ceram. Int. 39 (2013) 941–946.

[37] D. Segal, Chemical synthesis of ceramic materials, J. Mater. Chem. 7 (1997) 1297–1305.

[38] N.E. Leadbeater, Microwave Heating as a Tool for Sustainable Chemistry, CRC Press, 2010.

[39] J. Prado-Gonjal, R. Schmidt, D. Ávila, U. Amador, E. Morán, Structural and physical properties of microwave synthesized orthorhombic perovskite erbium chromite $ErCrO_3$, J. Eur. Ceram. Soc. 32 (2012) 611–618.

[40] K.J. Rao, B. Vaidhyanathan, M. Ganguli, P.A. Ramakrishnan, Synthesis of inorganic solids using microwaves, Chem. Mater. 11 (1999) 882–895.

[41] B.L. Hayes, Microwave Synthesis: Chemistry at the Speed of Light, CEM Pub, 2002.

[42] L.-Y. Meng, B. Wang, M.-G. Ma, K.-L. Lin, The progress of microwave-assisted hydrothermal method in the synthesis of functional nanomaterials, Mater. Today Chem. 1 (2016) 63–83.

[43] Z. Zhou, Y. Deng, Kinetics study of ZnO nanorod growth in solution, J. Phys. Chem. C 113 (2009) 19853–19858.

[44] R. Wahab, Y.-S. Kim, K. Lee, H.-S. Shin, Fabrication and growth mechanism of hexagonal zinc oxide nanorods via solution process, J. Mater. Sci. 45 (2010) 2967–2973.

[45] E. Novitskaya, J.P. Kelly, S. Bhaduri, O.A. Graeve, A review of solution combustion synthesis: an analysis of parameters controlling powder characteristics, Int. Mater. Rev. 66 (2021) 188–214.

[46] S.-X. Song, Z. Wang, G.-P. Shi, Heating mechanism of spark plasma sintering, Ceram. Int. 39 (2013) 1393–1396.

[47] J. Rodríguez-Carvajal, Recent advances in magnetic structure determination by neutron powder diffraction, Phys. B Condens. Matter 192 (1993) 55–69.

[48] P.L. Dulong, A.-T. Petit, Recherches sur quelques points importans de la theorie de la chaleur, 1819.

[49] D. Feng, Z.-H. Ge, D. Wu, Y.-X. Chen, T. Wu, J. Li, J. He, Enhanced thermoelectric properties of SnSe polycrystals via texture control, Phys. Chem. Chem. Phys. 18 (2016) 31821–31827.

[50] Asfandiyar, T.-R. Wei, Z. Li, F.-H. Sun, Y. Pan, C.-F. Wu, M.U. Farooq, H. Tang, F. Li, B. Li, J.-F. Li, Thermoelectric SnS and SnS-SnSe solid solutions prepared by mechanical alloying and spark plasma sintering: anisotropic thermoelectric properties, Sci. Rep. 7 (2017) 1–7.

[51] D. Feng, Z.-H. Ge, Y.-X. Chen, J. Li, J. He, Hydrothermal synthesis of SnQ (Q= Te, Se, S) and their thermoelectric properties, Nanotechnology 28 (2017) 455707.

[52] L. Xie, D. He, J. He, SnSe, the Rising Star Thermoelectric Material: a New Paradigm in Atomic Blocks, Building Intriguing Physical Properties, Materials Horizons, 2021.

[53] J. Gainza, F. Serrano-Sánchez, J.E. Rodrigues, Y. Huttel, O.J. Dura, M.M. Koza, M. T. Fernández-Díaz, J.J. Meléndez, B.G. Márkus, F. Simon, High-performance n-type SnSe thermoelectric polycrystal prepared by arc-melting, Cell Rep. Phys. Sci. 1 (2020) 100263.

[54] Y.-M. Han, J. Zhao, M. Zhou, X.-X. Jiang, H.-Q. Leng, L.-F. Li, Thermoelectric performance of SnS and SnS–SnSe solid solution, J. Mater. Chem. 3 (2015) 4555–4559.

[55] Asfandiyar, B. Cai, L.-D. Zhao, J.-F. Li, High thermoelectric figure of merit ZT> 1 in SnS polycrystals, J. Mater. 6 (2020) 77–85.

[56] J. Mayandi, R. Madathil, C. Abinaya, K. Bethke, V. Venkatachalapathy, K. Rademann, T. Norby, T. Finstad, Al-doped ZnO prepared by co-precipitation method and its thermoelectric characteristics, Mater. Lett. 288 (2021) 129352.

[57] K.H. Jung, S.M. Choi, C.H. Lim, W.S. Seo, H.H. Park, Phase analysis and thermoelectric properties of $Zn_{1-x}M_xO$ (M= Al, Ga) samples, Surf. Interface Anal. 44 (2012) 1507–1510.

[58] M. Mohammed, I. Sudin, A.M. Noor, S. Rajoo, M. Uday, N.H. Obayes, M.F. Omar, A review of thermoelectric ZnO nanostructured ceramics for energy recovery, Int. J. Eng. Technol. 7 (2018) 27–30.

[59] P. Mele, H. Kamei, H. Yasumune, K. Matsumoto, K. Miyazaki, Development of thermoelectric module based on dense $Ca_3Co_4O_9$ and $Zn_{0.98}Al_{0.02}O$ legs, Met. Mater. Int. 20 (2014) 389–397.

[60] T. Olorunyolemi, A. Birnboim, Y. Carmel, O.C. Wilson Jr., I.K. Lloyd, S. Smith, R. Campbell, Thermal conductivity of zinc oxide: from green to sintered state, J. Am. Ceram. Soc. 85 (2002) 1249–1253.

[61] J. Liu, C. Wang, W. Su, H. Wang, P. Zheng, J. Li, J. Zhang, L. Mei, Enhancement of thermoelectric efficiency in oxygen-deficient $Sr_{1-x}La_xTiO_{3-\delta}$ ceramics, Appl. Phys. Lett. 95 (2009) 162110.

[62] J. Sun, D.J. Singh, Thermoelectric properties of n-type $SrTiO_3$, Apl. Mater. 4 (2016) 104803.

[63] Y. Yin, B. Tudu, A. Tiwari, Recent advances in oxide thermoelectric materials and modules, Vacuum 146 (2017) 356–374.